# Investigation of the Influence of Different Flapping Wing Motion Characteristics on Aerodynamic Parameters under Incoming Flow

Z. Guo[1], R. Liu[2], S. Zheng[3], J. Xu[1] and J. Chang[1†]

*1 College of Mechatronics Engineering, North University of China, Taiyuan 030051, China*
*2 Jinxi Industrial GroupCo, Ltd, Taiyuan, 030027, China*
*3 State-run Changhong Machinery Plant, Guilin, 541002, China*

†*Corresponding Author Email: changjl@nuc.edu.cn*

## ABSTRACT

There is high flight efficiency of flapping wing aircraft, and its hovering ability, wind loading rating, maneuverability and concealment are better than that of multi-rotor and fixed-wing aircraft. In this paper, the bionic flapping wing is taken as the research subject, and a complete motion process of the flapping wing is divided into four stages by numerical method under the condition of incoming flow. It is found that there is delayed stall mechanism of leading-edge vortex, wake vortex capture mechanism and rotating circulation mechanism in flapping wing flight. On this basis, the impact of flapping wing kinematic parameters on flapping wing aerodynamic characteristics is explored. The effects of different flapping motion parameters on flapping aerodynamic parameters are investigated from three perspectives, including flapping frequency, direction of flapping wing motion and trajectory of flapping wing. It is demonstrated that increasing the flapping frequency can result in an improvement in the lift resistance characteristics. The phase difference of flapping wing motion can affect the angle of attack state for airfoil during flapping. When the flapping frequency, amplitude, and phase difference are identical, there is minimal disparity in the lift characteristics among different trajectories. However, a substantial discrepancy arises in the drag coefficient. The axisymmetric of motion trajectory will also cause significant differences in the lift characteristics.

## 1. INTRODUCTION

The concept of microlight aircraft was first proposed in the research reported on future military technology (McMichael, 1997). Since then, a large amount of research on micro flapping wing aircraft have been conducted by many enterprises and universities. The theoretical research on flapping wing aerodynamics has been continued to deepen, and miniature flapping wing aircraft manufactured has become increasingly complex. Miniature flapping wing aircraft referred to an aircraft whose wings are capable of flap in a comparable manner to that observed in birds and insects. Lift and forward propulsion are generated by the use of flapping wing. Its maneuverability is flexible, flight efficiency is efficient, and concealment is good. It has broad application scenarios and value in both military and civilian fields, such as narrow space reconnaissance in urban counter-terrorism.

The influence of flapping wing motion function on insect aerodynamics were investigated by Shantanu S. Bhat through numerical simulation and experimental methods (Bhat et al., 2020). The motion functions of the experiment and numerical simulation were as follows:

$$\begin{cases} \phi(t) = \frac{\phi_A}{sin^{-1}K} sin^{-1}[K \sin(2\pi ft + \delta_\psi)] \\ \psi(t) = \frac{\psi_A}{tanh(C_\psi)} tanh[C_\psi \sin(2\pi ft)] \end{cases} \quad (1)$$

It was found that the effects of $K$ in the motion function on average lift coefficient ($\overline{C_L}$) and dynamic efficiency ($PE$: ratio of average lift coefficient to average dynamic coefficient) are different: lift coefficient will be maximized by a lower $K$ value and a higher $C_\psi$. When the value of $K$ is higher and the value of $C_\psi$ is about 3, $PE$ will be maximized.

The change of aerodynamic characteristics of flapping wings was when they changed from flapping motion to proposing motion through direct simulation

NOMENCLATURE

| | | | | |
|---|---|---|---|---|
| $C_{LA}$ | average lift coefficient | | $L$ | characteristic length |
| $C_{DA}$ | average drag coefficient | | $S$ | characteristic area |
| $C_L$ | lift coefficient | | $F_{lift}$ | lift force |
| $C_D$ | drag coefficient | | $F_{drag}$ | drag force |
| $\bar{C}_{L(T)}$ | periodic average lift coefficient | | $f$ | characteristic frequency |
| $\bar{C}_{D(T)}$ | periodic average drag coefficient | | $PE$ | ratio of average lift coefficient to average dynamic coefficient |
| $\nabla\vec{u}$ | displacement velocity of the mesh | | $U_{ref}$ | characteristic velocity |
| $\gamma$ | diffusion coefficient | | $\alpha$ | rotation angle of the airfoil |
| $u$ | fluid velocity vector | | $\phi$ | phase of the rotation angle |
| $p$ | flow field pressure | | $\alpha_\alpha$ | rotation angle amplitude |
| $v$ | viscosity coefficient of fluid motion | | $\alpha_0$ | initial angle |
| $h$ | horizontal displacement of the airfoil center of gravity | | | |

numerical method (Gonzalo et al., 2018). It was established that the spanwise zone of leading-edge vortex separation was related to the flapping radius. For porpoising motion, leading-edge vortex separation initially occurred at the edge of half span, while for flapping motion, leading-edge vortex separation initially occurred near the tip of the wing.

It was found through the research of Wei Shyy that for a flapping wing with limited wingspan, the lifting force could be enhanced by augmenting the low-pressure zone caused by the wingtip swirl (Shyy et al., 2009). The leading-edge vortex was capable to be anchored, delayed or even prevented from falling off by the wingtip swirl. 2D and 3D numerical simulation were conducted on a flapping wing motion plate with aspect ratio of 4 and Reynolds number of 100 in hover state by Pat Trizila (Trizila et al., 2011). And it was ascertained that lift and power performance of flapping wing plate could be significantly affected by wingtip swirl. The leading-edge vortex could be interacted with the wingtip swirl to contribute to the generation of lift, but there was no additional power demand.

The contribution of flapping wing flexibility on the hovering and forward flight parameters was explored by Namhun Lee through numerical methods, and it was determined that the thrust force increased with the elevation in flapping frequency caused by flapping wing (Lee et al., 2018). The advance ratio was the reason for the thrust reduction of flexible flapping wings with high flapping frequencies. The effects of different types of warily interaction on micro flapping wing aircraft were studied numerically by Wee Beng Tay, and the results was shown that the highest lift was produced by the spanwise rigid and chordwise flexible wing but the least power required (Tay, 2017). Higher lift could be produced by more wings but higher drag produced and more power required.

Large Eddy Simulation (LES) technology was occupied to analyze 3D flapping wing with the low aspect ratio by Zhang Jiaolong, and it was found that the lift performance was continuously enhanced with the reduction of frequency (Jiaolong et al., 2017). Over the dimensionless time 0.2, the lift-drag performance of the flapping wing had been altered slightly by the frequency

reduction. The vortex structure around the wings of fruit flies and cicadas was surveyed by Hyeon Kyun Lee through the Intrusion Boundary Lattice Boltzmann Method (IB-LBM), and it was shown that there were differences in the vortex structure between fruit flies and cicadas (Lee et al., 2019). Because of the unique shape of the trailing-edge, the paddle wing would be unbalanced caused by the trailing-edge vortices produced by itself, then the RV-LEV-TEV1 cycle was developed from two trailing-edge vortices resulted by the paddle wing. The ground effect of the tandem flapping wing hovering on the inclined stroke plane was probed by Srinidhi N G through numerical methods, and it was found that the maximum upward lift and wake with eddy current would be produced by the in-phase stroke of the series wing, while the minimum force and wake would be produced by the reverse stroke and reduce the force fluctuation (Srinidhi & Vengadesan, 2017).

The Direct Numerical Simulation (DNS) method was acclimatized to study the effect of 3D effect of flapping wing motion on the behavior of flapping wings in tandem layout (Arranz et al., 2020). It was found that when aspect ratio $AR$=2 or 4, the interaction mechanism of the vortex structure between the leading edge and trailing edge wings in the three-dimensional case was similar to that in the two-dimensional case. However, the average thrust generated in the three-dimensional case of finite wingspan was lower than that in the two-dimensional case of infinite wingspan. And this reduction would advance with the increasing of aspect ratio, while this reduction was more obvious in the trailing edge wing.

The affection of uniform lateral incoming flow on aerodynamic characteristics was investigated by Jong-Seob Han through experiments, and it was found that there is a favorable impact on the stability lateral flight through the interaction between wings (Han et al., 2019).

The influence of mass and chord direction flexibility on performance of two-dimensional flapping wings was released by Mathieu Olivier, and it was found that: when the pressure- inertia ratio was high, there was the best flexibility, by which the efficiency of flapping wings would be maximized (Olivier & Dumas, 2016). By contrast, when the pressure-inertia ratio was low, the efficiency would be systematically reduced by the

flexibility. For any pressure-inertia ratio, the cycle average velocity would be also decreased within an increase in flexibility.

An X-wing flapping mechanism with symmetrical wing flapping was designed by Huan (Xiansheng et al., 2023). The optical motion capture system and wind tunnel were used to conduct motion tests on the flapping mechanism, and its reliability was analyzed from the aspects of flapping angle amplitude, flapping frequency, lift generated and motor operating states.

The design, aerodynamic behavior, and control mechanisms of a butterfly-inspired flapping wing robot had been investigated by Haifeng Huang (Huang et al., 2024). A combination of experimental and computational methods had been used to analyze the aerodynamic forces produced by the flapping wings, deepening the understanding of fluid dynamics. The implementation of flight control algorithms, enabling stable flight under various conditions, was explored. Based on the constructed motion model, it was demonstrated that frequency and angle offset modulation were significant affected on flight altitude and course control, which had been validated. Additionally, the vortex evolution during level flight was investigated, revealing its consistency with variations in aerodynamic forces.

A comprehensive review of the latest advances in the design of bio-inspired flapping-wing aerial vehicles (BFAV) was presented in this paper by Dongfu Ma (Ma et al., 2024). The overall design, flapping-wing design, drive system design, and prototype integrated design were mainly focused on in the review, with the aim of having the solutions and methods adopted in the design process of each system elucidated from the perspective of aviation designers. In addition, the future development directions and challenges faced in this field were also analyzed.

Strategies to enhance lift generation in flapping wing systems through manipulation of tip vortices were studied by Bruce Ruishu Jin (2024). It examined the role of shear layers and vortex dynamics in improving aerodynamic performance during wing flapping. By analyzing the interactions between wingtip vortices and surrounding airflow, methods were proposed to optimize these vortices for increased lift. It had been found that at Reynolds numbers of 1000 and 5000, the blowing jet downstream of the trailing edge was the most significantly affected on enhancing lift production among all configurations by increasing the net circulation on the wing. A more extensive and stronger vortex tube (TV) was generated by the increase in the mass flux of the shear layer near the wing tip.

The use of wake monitoring techniques to assess aerodynamic loads on airfoils operating at low Reynolds numbers was evaluated by Verma and Kulkarni (2024). The relationship between wake behavior and aerodynamic performance was analyzed, particularly in conditions where traditional load measurement methods were less effective. It was observed that at a low angle of attack, the magnitude of drag remained almost constantly and then increased rapidly. At the same Reynolds number, a higher value of the maximum lift-to-drag ratio was presented by the E214 airfoil compared with the S5010 airfoil.

The flapping wing aircraft is a new concept of bionic aircraft. Extensive investigation had been implemented and many excellent results were achieved. The current related research on the flapping wing can be simply summarized as the contribution of the motion parameters and shaping and development of vortex structure on aerodynamic characteristics. The flight mechanism of flapping wing aircraft is apart from that of conventional fixed wing aircraft, and the current theoretical research of flapping wing flight at low Reynolds number still are required to develop. Consequences of flapping wing motion parameters on aerodynamic characteristics at low Reynolds number are mainly explored by numerical methods in this article, including flapping frequency, flapping direction and trajectory. Then the rules are analyzed and summarized.

## 2. NUMERICAL METHOD

With the advancement of computer software and hardware, as well as the proposal and verification of advanced algorithms and physical models, numerical methods are used to study complex flow fields gradually because of its advantages of saving time and money. For that reason, numerical methods are chosen for this essay to investigate the structure and aerodynamic characteristics of flapping wing flow fields.

### 2.1 Model

The flapping wing model is represented in Fig. 1, by which non-structural hybrid grids is adopted. The airfoil string length is $h$, as well as the computational area is
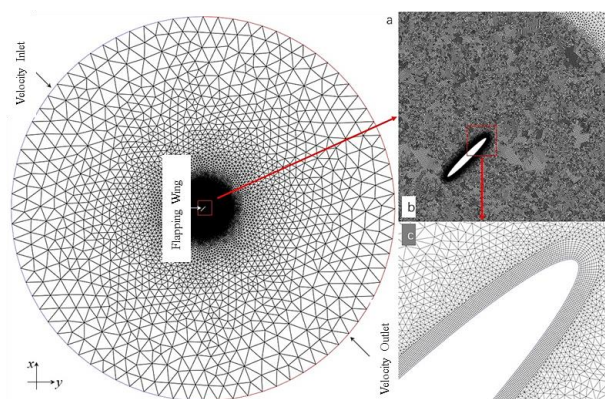


**Fig. 1 Flow field mesh**

circular, the radius length is $25h$. The left semicircle is the velocity inlet, the right semicircle is the pressure outlet. And the wall non-slip boundary condition is adopted by the surface of the airfoil, that is, the surface fluid velocity is the same as the movement velocity of the airfoil. The governing equations are discretized by the second order upwind scheme and the second order central difference scheme respectively. The governing equation is solved by using the PISO algorithm coupled with pressure and velocity, and the CFL number is selected as 1.

The finite volume method (FVM) is one of the most widely used discretization techniques in computational fluid dynamics (CFD). Based on the control volume formulation of analytical fluid dynamics, the computational domain is divided into multiple control volumes (i.e., cells or elements) in the first step of FVM, where the variables of interest are located at the centroids of the control volumes. The differential form of the governing equations is then integrated over each control volume (which is quite similar to the control volume method). Interpolation profiles are assumed to describe the variations of the relevant variables between the centroids of the cells. The resulting equations are called discretized or discretization equations. In this way, the conservation principle of variables within the control volumes is expressed by the discretization equations.

Three methods for updating the grids in the deforming regions according to the motion defined at the boundaries are provided by Fluent:

(a) Layering. In the prismatic (hexahedral and/or wedge-shaped) grid regions, cell layers adjacent to the moving boundaries can be added or deleted by the dynamic layering method based on the height of the layers adjacent to the moving surfaces.

(b) Smoothing. When the grids in the regions with moving and/or deforming boundaries are adjusted by using smoothing, the internal nodes of the grids will be moved, but the number of nodes and their connectivity will not be changed. In this way, the motion of the boundaries is "absorbed" by the internal nodes.

(c) Remeshing. It is necessary to determine whether the set skewness or size criteria are met when the grids move or deform before this operation is executed. If not, the grid cells or grid faces will be locally reconstructed. If the new cells or faces meet the criteria, the grid will be locally updated using the new cells (by interpolating the calculation results from the old cells). Otherwise, the new cells will be discarded and the old cell grids will be retained.

In this essay, the diffusion based smoothing method is named to update the mesh. With regard to diffusion-based smoothing, grid movement is controlled by the Diffusion equation, which is shown as follows:

$$\nabla \cdot (\gamma \nabla \vec{u}) = 0 \qquad (2)$$

In Eq. (2), $\nabla \vec{u}$ is the displacement velocity of the grid and $\gamma$ is the diffusion coefficient, which can be applied to govern the influence of the boundary motion on the internal grid movement.

## 2.2 Boundary Conditions

When birds and insects fly with flapping wings in nature, the air flow speed in the flow field is low (Mach number is about 0.02), and the characteristic length of the gas is relatively small compared with the flapping wing size, so the flow field can be assumed to be incompressible flow. The Reynolds number of flow field is small, and a new shear layer is generated by each flapping on the wing surface, which can be simplified to laminar flow. Thus, the control equation of flapping wing flow field can be simplified to the incompressible Navier-Stokes equation, as follows:

$$\nabla \cdot u = 0 \qquad (3)$$

$$\frac{\partial u}{\partial t} + u \cdot \nabla u = -\frac{1}{\rho} \nabla p + \nu \nabla^2 u \qquad (4)$$

Where $u$ is fluid velocity vector, $p$ is flow field pressure, $\nu$ is viscosity coefficient of fluid motion.

Reynolds number $Re$ is used to characterize relative size of fluid inertia force and viscous force in flow field. The smaller the Reynolds number is, the more significant the influence of viscous force is, which is defined as follows:

$$Re = \frac{U_{ref} L}{\nu} \qquad (5)$$

Where $L$ is the characteristic length, $U_{ref}$ is characteristic velocity and $\nu$ is kinematic viscosity of the fluid. When the incoming velocity is not zero, $U_{ref}$ is taken as the incoming flow, and when $U_{ref}$ is zero, maximum flapping velocity is taken as the $U_{ref}$.

The unsteady degree of the flow field is represented by Strouhal number $St$, which is defined as follows:

$$St = \frac{Lf}{U_{ref}} \qquad (6)$$

Where $f$ is characteristic frequency and $L$ is characteristic length. In this paper, the characteristic frequency is flapping frequency, and the characteristic length is chord-length of airfoil.

For forward flapping wing model, advance ratio $J$ is also an essential element by which flow field characteristics is determined. There is considerable consequence on aerodynamic performance by $J$. Its specific definition is as follows:

$$J = \frac{U_\infty}{U_{ref}} \qquad (7)$$

Where $f$ is the incoming velocity and $U_{ref}$ is the reference characteristic velocity. Lift coefficient $C_L$, periodic average lift coefficient $\bar{C}_{L(T)}$ are defined as follows:

$$C_L = \frac{F_{lift}}{\frac{1}{2}\rho u^2 S} \qquad (8)$$

$$\bar{C}_{L(T)} = \frac{\int_{nT}^{(n+m)T} C_L dt}{mT} \qquad (9)$$

In the Eq. (8) and (9), $\rho$ is fluid density, $S$ is characteristic area, and $F_{lift}$ is lift force received by the object. In this paper, the lift force is positive along the

(a)



(b)



(c)
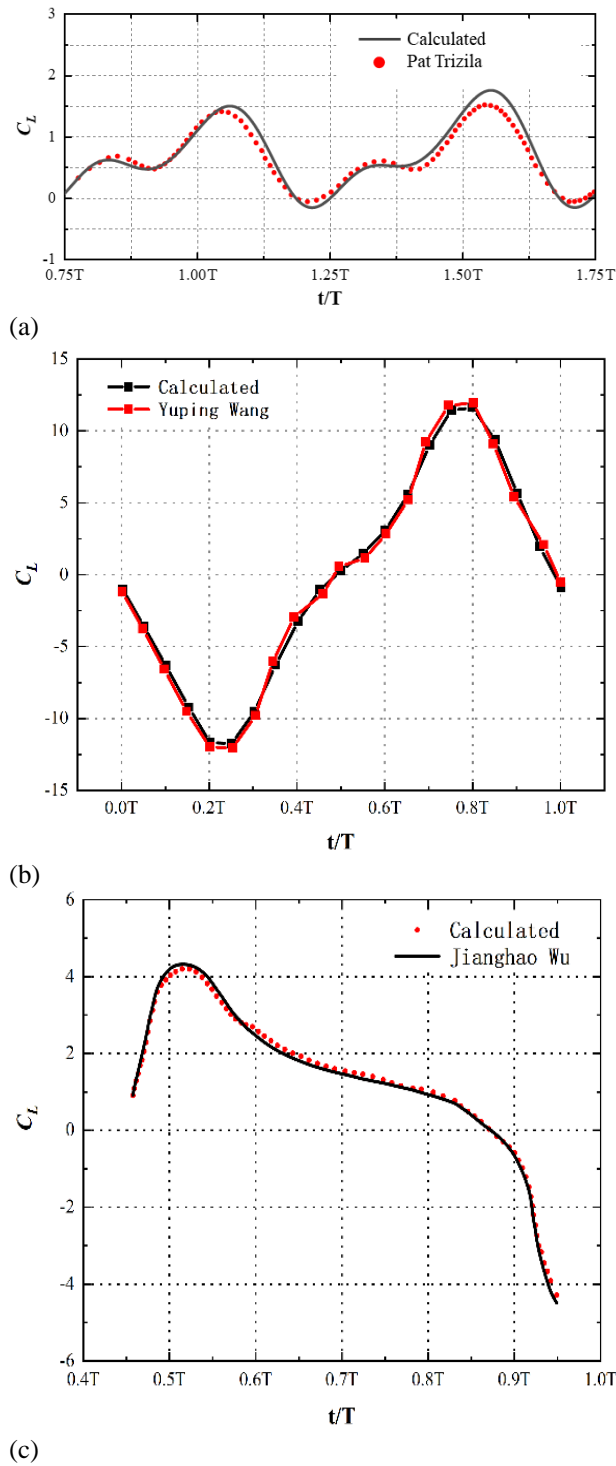
**Fig. 2 Comparison of lift coefficient results**

positive of $y$, $u$ is the characteristic velocity. $u$ is the maximum translation velocity when hovering. $u$ is the flow velocity when flying forward, and $m$ and $n$ are positive integers.

Drag coefficient $C_D$ , periodic average drag coefficient $\bar{C}_{D(T)}$ is defined as follows:

$$C_D = \frac{F_{drag}}{\frac{1}{2}\rho \, u^2 S} \tag{10}$$

$$\bar{C}_{D(T)} = \frac{\int_{nT}^{(n+m)T} C_D dt}{mT} \tag{11}$$

**Table 1 Minimum mesh size and number of nodes and cells**

| Type | Minimum mesh size(mm) | Nodes | Cells |
|---|---|---|---|
| Grid 1 | 1e-5 | 81291 | 142100 |
| Grid 2 | 1e-5 | 100445 | 189568 |
| Grid 3 | 5e-7 | 149265 | 255235 |

In the Eq. (10) and (11), $\rho$ is fluid density, $S$ is characteristic area, $F_{drag}$ is drag force of the object, and the drag in this paper is positive along the positive of $x$.

## 2.3 Accuracy and Grid Independence Verification

In this paper, the flow field is numerically solved through FVM. The effects of the motion and the structure parameters on aerodynamic characteristics are investigated.

First, to ensure the accuracy of the method presented in this paper, the aerodynamic characteristics of a rigid flapping wing at $Re$=100, computed using the proposed method, are first compared with those of Pat Trizila (Trizila et al., 2011). Next, the structure of the dragonfly forewing is simplified by neglecting the variations in the wing veins and membrane along the spanwise and chordwise directions. Flow field simulations of a pair of symmetric flexible flat-plate wings at $Re$=1600 are carried out using the proposed computational method and code, with the results compared to those of Wang et al. (2022). Finally, the aerodynamic characteristics of a rotating wing at $Re$ =1500, computed using the proposed method, are compared with those of Wu et al. (2019). The comparison results are shown in Fig. (2).

Grid 1, 2, and 3 are triangular unstructured grid whose minimum mesh size and number of nodes and cells are shown in Table 1. Grid 2 is based on grid 1 to encrypt the $3h$ diameter area around the flapping wing. The results of the lift coefficients in three grids are shown in Fig. 3 below. It is found that the error of Grid 1 with reference to Grid 2 is 6.2% and the error of Grid 2 according to Grid 3 is 1.09%. With the aim of accuracy and computing resources, Grid 2 is constituted as computational grid of flow field.

## 3. RESULTS AND ANALYSIS

In this paper, the motion function of flapping wing under the influence of the lift mechanism, frequency and phase difference are as follows:

$$\begin{cases} h(t) = h_a \sin(2\pi ft) \\ \alpha(t) = \alpha_0 - \alpha_a \sin(2\pi ft + \phi) \end{cases} \tag{12}$$

The motion diagram of flapping wing is depicted in Fig. 4 below. Flapping structure parameters and flapping frequency are shown in Table 2. A flapping stroke is included by single flapping to the left and right. They are symmetrical motions, so the flapping stroke is regarded as the minimum unit of periodic motion of the flapping wing. In this part, the aerodynamic characteristics with incoming flow $u$ =0.6m/s are investigated. And the flow field is numerically solved using the FVM, where $Re \approx 205$,
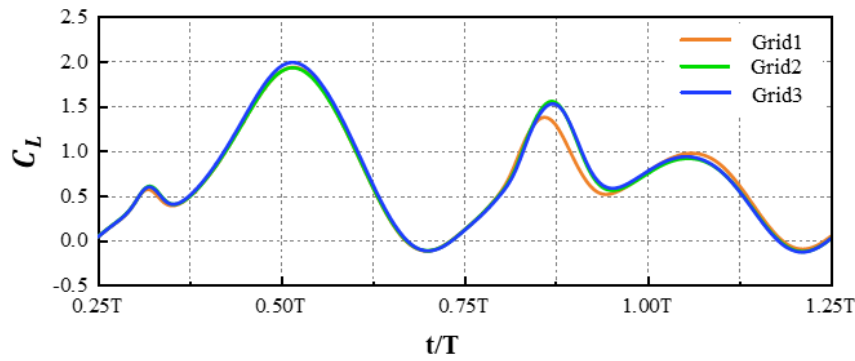
**Fig. 3 Comparison of lift coefficient results of flapping wing with different grids**
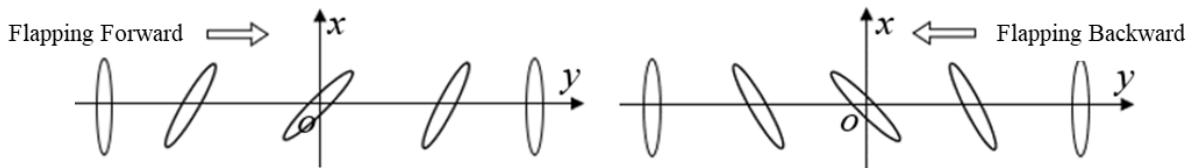


**Fig. 4 Schematic diagram of flapping wing movement**
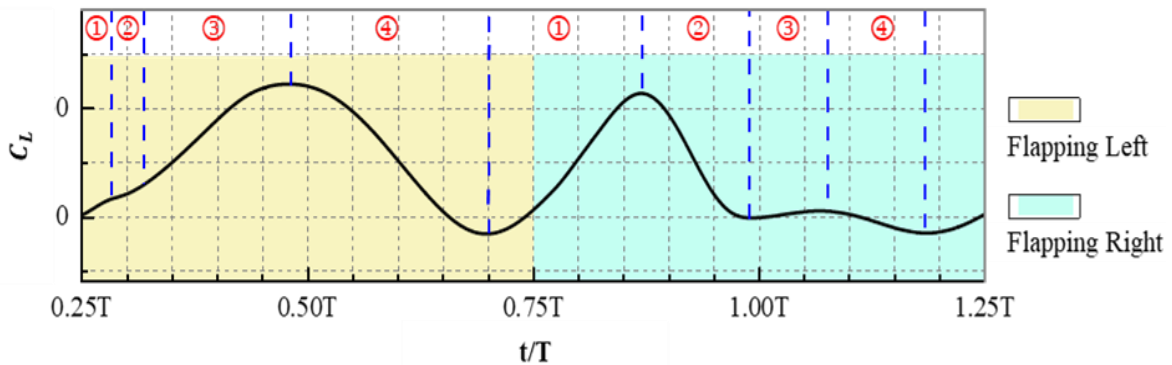


**Fig. 5 Lift coefficient curve of flapping wing**

**Table 2 Structural parameters and flapping frequency**

| Shape | Elliptical |
|---|---|
| Chord-length | $h_a$ |
| $\alpha_0$ | 45° |
| $\alpha_\alpha$ | 90° |
| $\phi$ | 90° |

$St \approx 0.83$, $J \approx 0.19$. As shown in Fig. 5 below, it is the lift coefficient curve of flapping wing with longitudinal incoming flow. In the case of longitudinal incoming flow, the travel of the flapping wing in a flapping process is divided into four stages: (1) wake vortex capture increase, (2) leading-edge vortex shedding caused by rotation circulation mechanism, (3) delayed stall mechanism of leading-edge vortex, and (4) leading-edge vortex shedding caused by translation motion.

(1) Capture and enhance of the wake vortex. A new leading-edge vortex is emanated amid rotating process of flapping wing. After previous stroke is completed,

flapping wing then flaps to the other end, during which the wake vortex dropped off in the process (4) is captured. The kinetic energy of the wake vortex is absorbed, by which leading-edge vortex and low-pressure area of upper-wing surface are made stronger.

(2) Leading-edge vortex shedding caused by rotation mechanism. The flapping wing continues to flapping to the other end, the rotation speed becomes slower, and the translational velocity becomes faster. The leading-edge vortex derived by rotation falls off from the upper airfoil, low-pressure area of upper airfoil weakens, lift force decreases, and lift coefficient curve begins to drop until new leading-edge vortex is produced.

(3) Delayed stall mechanism of leading-edge vortex. After (2), flapping wing continues to flap to the other end, generating new leading-edge vortex, which is dominated by translational motion and provides kinetic energy for leading-edge vortex. Newly generated leading-edge vortex is attached to upper-wing surface and low-pressure area on upper-wing surface is generated, which makes the lift force increase, and lift coefficient curve climbs upward again at this stage.
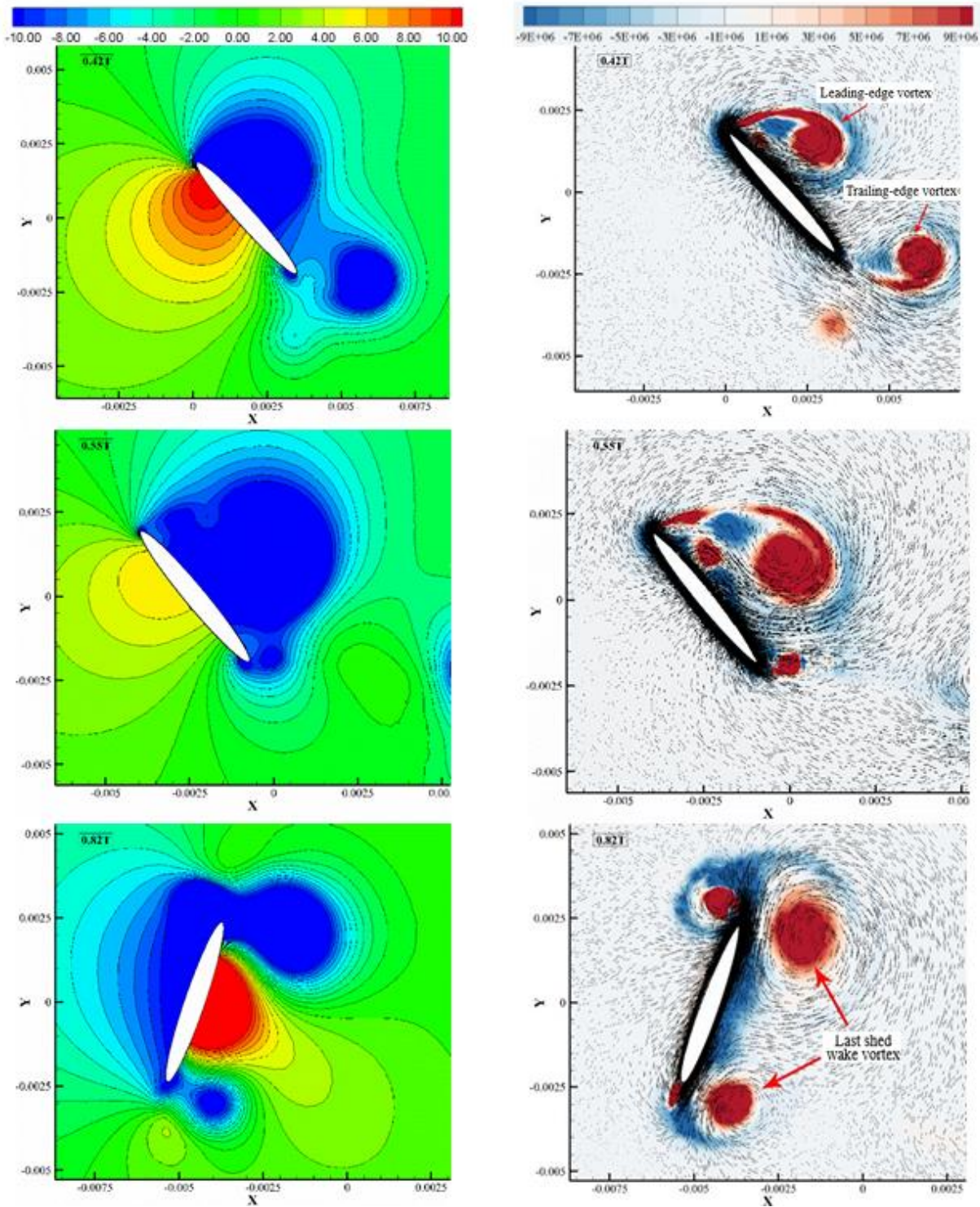
**Fig. 6 Flow field contours of flapping wing, pressure contour on the left and vorticity contour on the right (Q criterion), *Re* = 205**

(4) Leading-edge vortex shedding caused by translation motion. When wing moves to the other end, the translation speed decreases, the rotation speed increases, leading-edge vortex and trailing-edge vortex shed off. Low-pressure area of upper-wing surface becomes weaker, lift force drops, and the lift coefficient curve begins to decline, and it continues to decline with the decreasing strength of leading-edge vortex until the next lift mechanism begins.

It is found in this paper that the wake vortex capture mechanism is closely related to the delayed stall mechanism of leading-edge vortex. If the leading-edge vortex generated through the delayed stall mechanism of leading-edge vortex is shed prematurely, it will lead to the situation that the shed leading-edge vortex cannot be fully utilized by the trailing vortex capture mechanism, and the lift coefficient is decreased. The second stroke λ in Fig. 6 is the case as described above. (1),(2) and (3) in the second

stroke (the light blue area) of Fig. 6 are the situations described above.

Generally speaking, a relatively large and complete leading-edge vortex will be formed by the delayed stall mechanism of leading-edge vortex. However, in simulations, it sometimes sheds prematurely, and then a second, smaller leading-edge vortex is produced by the delay stall mechanism. A smaller leading-edge vortex is also captured through wake vortex capture mechanism. Compared with a complete leading-edge vortex being captured, the lift enhancement effect is significantly reduced. This situation should not be allowed to occur in the flapping flight of birds and insects. When a flapping wing aircraft is being designed, attention should be paid to this point, and this situation must be avoided. The cloud diagram of the numerical calculation results of the flapping wing flow field is shown in Fig. 6 below.

At 0.42T in Fig. 6, it is exactly at the moment of the delayed stall mechanism of leading-edge vortex. The upper surface of the wing is attached by the leading-edge vortex due to the angle of attack of the airfoil, a low-pressure area is formed on the upper surface and the lift of the flapping wing is increased. A low-pressure area is produced at the trailing edge of the flapping wing by the trailing-edge vortex, which has a relatively minor impact on the low-pressure area on the upper surface of the flapping wing. It can also be seen from the figure that a trailing-edge vortex is captured by the flapping wing, by which the low-pressure area at the trailing edge of the flapping wing is enhanced.

At 0.55T in Fig. 6, the intensity of the leading-edge vortex keeps increasing while its adhesiveness is decreased. Eventually, the upper surface of the wing is separated and shed from by the leading-edge vortex. The intensity of the low-pressure area on the upper surface is decreased with the shedding of the leading-edge vortex, and the lift is gradually reduced.

At 0.82T and 0.92T in Fig. 6, it can be observed that the rotation directions of the captured leading-edge vortex and the leading-edge vortex formed by rotation are opposite. The fluid velocity at the leading edge is accelerated through the captured leading-edge vortex. Nevertheless, the intensity of the captured leading-edge vortex is so large that the intensity of the leading-edge vortex created by rotation is increased rapidly, and its adhesiveness is decreased significantly. Ultimately, it is separated quickly.

The results of flow field are shown in Fig. 6, where interaction between the wake vortex capture mechanism and the leading-edge vortex delayed stall mechanism is. Old leading-edge vortex shed by previous flapping is captured though the wake vortex capture mechanism completely, with obvious lifting effect. But it is found that new leading-edge vortex generated by the subsequent flapping will be weaken, and the captured leading-edge vortex will interfere with next leading-edge vortex, making its strength weak and unstable. Certain energy is consumed by new leading-edge vortex for overcoming interference of old leading-edge vortex on the air flow, because direction of captured old leading-edge vortex

vector is opposite to that of the newly generated leading-edge vortex vector. The capture of next wake vortex will be affected by newly formed leading-edge vortex, so the two mechanisms continue to influence each other during the flapping wing process. From the energy point of view, the kinetic energy of the wing of a flapping wing stroke is mainly converted into air kinetic energy with lifting effect through these two mechanisms (a part of the kinetic energy is converted into internal energy consumption by friction, but the proportion is small and can be ignored). When the air kinetic energy transformed by one mechanism is larger, the air kinetic energy transformed by the other mechanism will be smaller.

In terms of the lift mechanism, the decrease in the lift coefficient is all related to the shedding of the leading-edge vortex. The pressure states of the upper and lower wing surfaces can be changed by rotation, with the low-pressure areas being transformed into high-pressure areas and vice versa. Meanwhile, the leading-edge vortex is generated by rotation and the lift of the wing surface is increased. The leading-edge vortex shed in the previous stroke can be captured through the wake vortex capture mechanism and the low-pressure area on the upper wing surface is enlarged.

The leading-edge vortex can be created by both rotation and translation, and it is related to the dominant motion. If the dominant motion is changed, the generated leading-edge vortex will not be able to obtain energy, the adhesiveness of the leading-edge vortex to the wing surface will be declined and it will be shed. The next lift mechanism will be affected by the previous lift mechanism.

### 3.1 Influence of Flapping Frequency

The impact of flapping frequency on aerodynamic characteristics is mainly studied when incoming flow $u$ is 0.6m/s. The structural parameters are same with Table 2. And the frequency $f$ are 25Hz, 50Hz, 100Hz and 150Hz respectively.

The lift coefficient curves of flapping wings with different frequencies are obtained from computational data, as revealed in Fig. 7. Average lift coefficient line curves of flapping wings with different frequency periods are obtained through data processing, as illustrated in Fig. 8.

It can be considered from Fig. 7 that: 1) The lift coefficient curve corresponding to each flapping wing frequency is above $x$ most of time, and $C_L$ is positive. In a small part of the time, it is negative below $x$ at the end of the flapping wing stroke. 2) Along $y$, $C_L$ of $f$=250Hz is generally at the top, followed by the lift coefficient curve of $f$=100Hz and $f$=50Hz, and the lift coefficient curve of $f$=25Hz is at the bottom. As the frequency increases, the lift coefficient increases. 3) Flapping wing curve changes in a period are roughly the same. As can be seen from Fig. 8, when the $f$ is 25Hz, 50Hz, 100 Hz, 150Hz, its periodic average lift coefficient is positive. As the $f$ increases from 25Hz to 150Hz, $\bar{C}_{L(T)}$ increases.
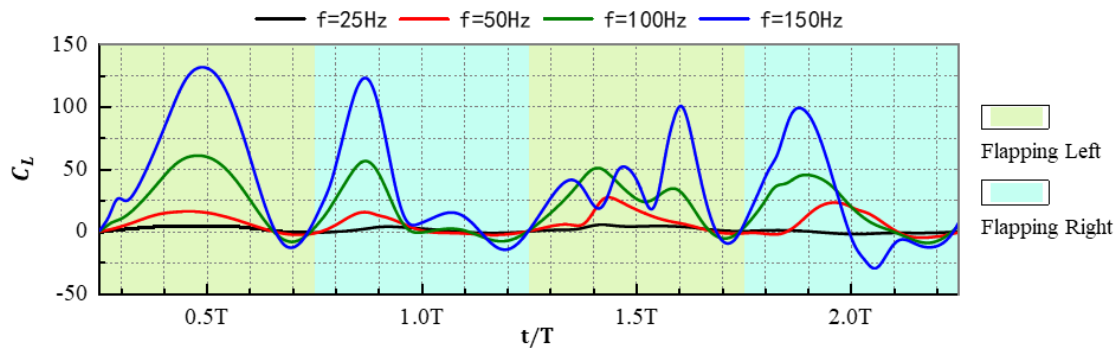
**Fig. 7 Lift coefficient curves at different frequencies**
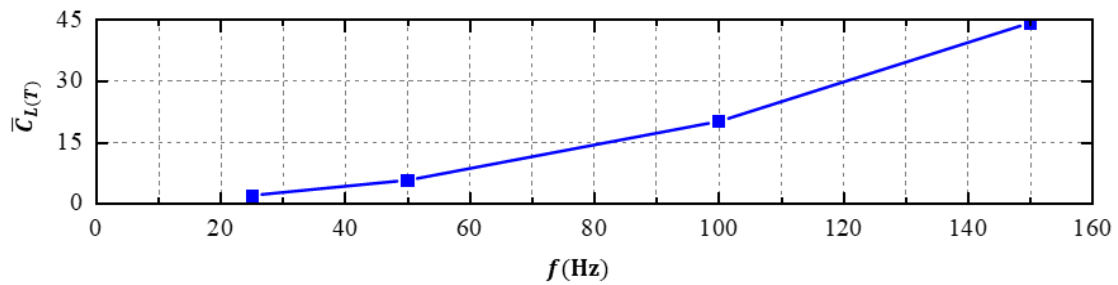


**Fig. 8 Periodic average lift coefficient of different frequency**
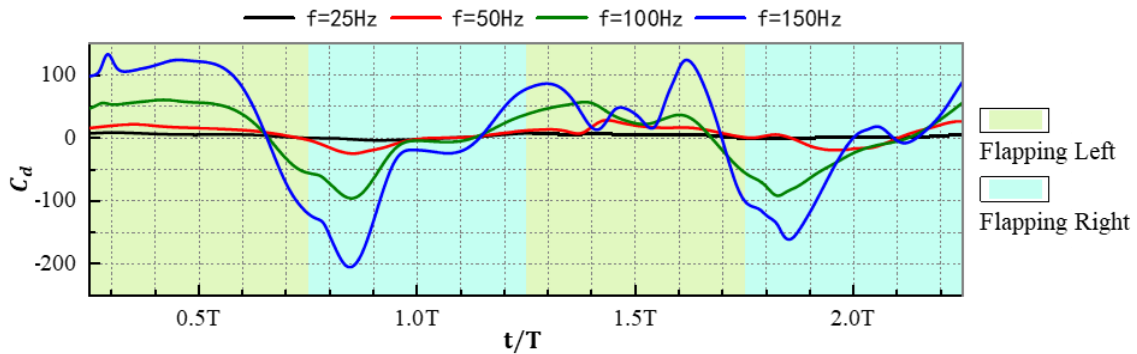


**Fig. 9 Drag coefficient curves at different frequencies**

Drag coefficient curves of flapping wings with various frequencies are regarded in Fig. 9, from which it can be seen that: 1) In this paper, the drag direction is positive to the right. During most of the time when the flapping wing flaps to the left, the drag coefficient is positive and the flapping wing is subjected to the drag to the right. During a small part of the time when the flapping wing stroke is over and the next flapping stroke is started, the drag coefficient is negative and the drag direction is left. A flapping to the left is similar, except that the force is in the opposite direction. 2) No matter flapping to the left or to the right, curve of $f$=150Hz is farthest from $x$ most of time, and absolute value of corresponding $y$ is largest, and the drag is the largest, followed by $f$=100Hz, $f$=50Hz. It is closest to the $x$ wheelbase for $f$=25Hz, and absolute value of corresponding $y$ is the smallest when the drag is the least. As frequency increases, the drag coefficient of flapping wing increases. 3) A comparison of

Fig. 7 and Fig. 9, it is possible to determine that peak and valley values of curves of lift coefficient and drag coefficient are same, and trend of the absolute value of the curves is the same. Drag force and lift force are the components of the resultant force on flapping wing along the $x$ and $y$. As resultant force increases, the component also increases, and $C_L$ and $C_D$ increase simultaneously. The periodic average drag coefficients of different frequencies are shown in Fig. 10. With the development of flapping frequency, periodic average drag coefficients of flapping wings also increase. If the periodic average drag coefficient of flapping wings is positive, the force effect during flapping period is equivalent to the drag to the right of the period, which indicates that the flapping wings cannot fly forward according to the given incoming flow speed.

The flow field with different frequencies at t=0.43T is portrayed in Fig. 11. It is obvious that when flapping wing
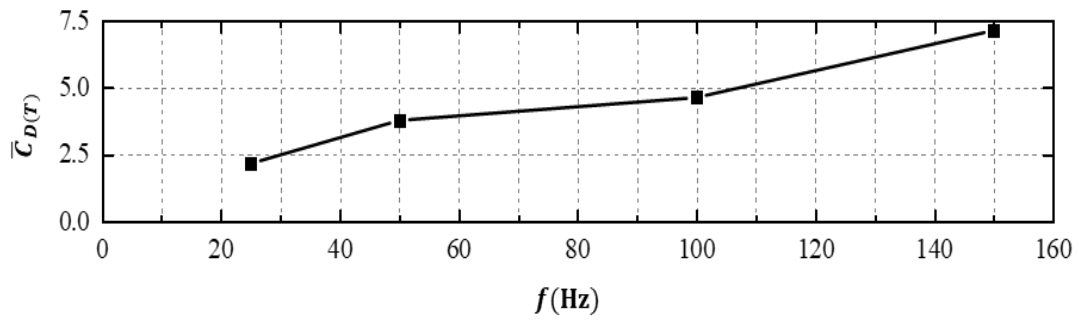
**Fig. 10 Average drag coefficient of different frequency periods**
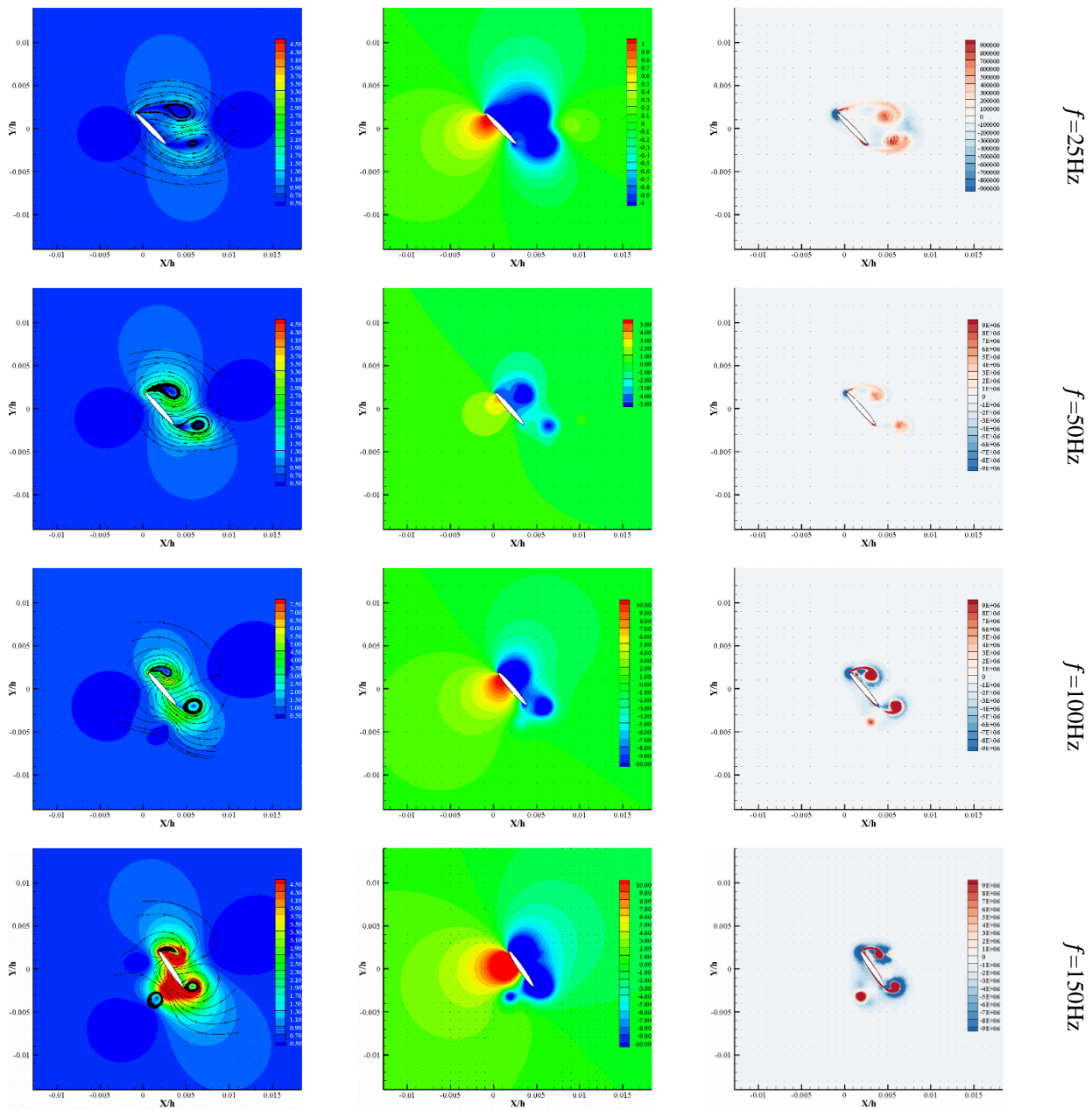


**Fig. 11 Flow field when t=0.43T, velocity contour on the left, intermediate pressure contour and vorticity contour on the right (Q criterion)**

flaps to the left, there is a leading-edge vortex attached to upper airfoil and low-pressure area is engendered at the leading-edge. Then trailing-edge vortex is generated at trailing edge and low-pressure area is generated near trailing edge of the airfoil. With the rise in flapping wing frequency, the intensity of leading-edge vortex and trailing-edge vortex is also increasing, and the corresponding low-pressure region is also increasing. At this moment, the flapping wings are in the state of increasing leading-edge vortex delay stall mechanism.

The flow field of flapping wing with different frequencies at t= 0.83T is reflected in Fig. 12. It is possible to observe that flapping wing is flapping to right, and there is leading-edge vortex at leading edge of flapping wing and trailing-edge vortex at trailing edge of flapping wing. At this moment, the wake vortex that fell off in the previous stroke at leading edge and trailing edge is also apprehended by flapping wing, making low-pressure area at leading edge and trailing edge of flapping wing stronger. As development of frequency, leading-edge vortex, trailing-edge vortex and captured wake vortex are all stronger, and corresponding low-pressure region is also stronger. At that moment, flapping wing is in the state of wake vortex capture mechanism. It is shown on the above phenomenon that, in the case of incoming flow, the strength and adhesion of leading-edge vortex and trailing-edge vortex can be augmented by increasing frequency, thus the aerodynamic characteristics is improved.
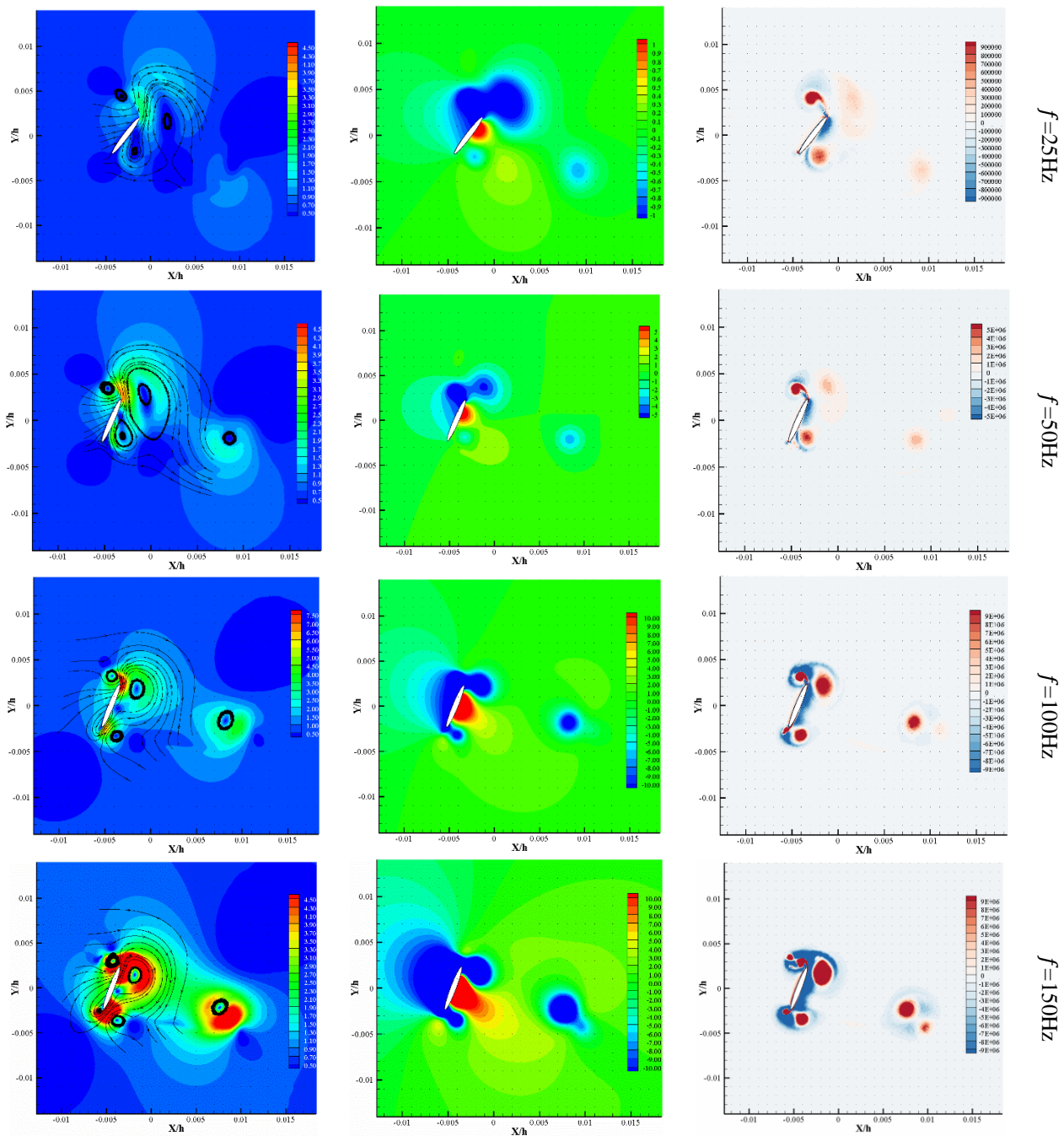


**Fig. 12 Flow field contour when t=0.83T, velocity contour on the left, intermediate pressure contour and vorticity contour on the right (Q criterion)**
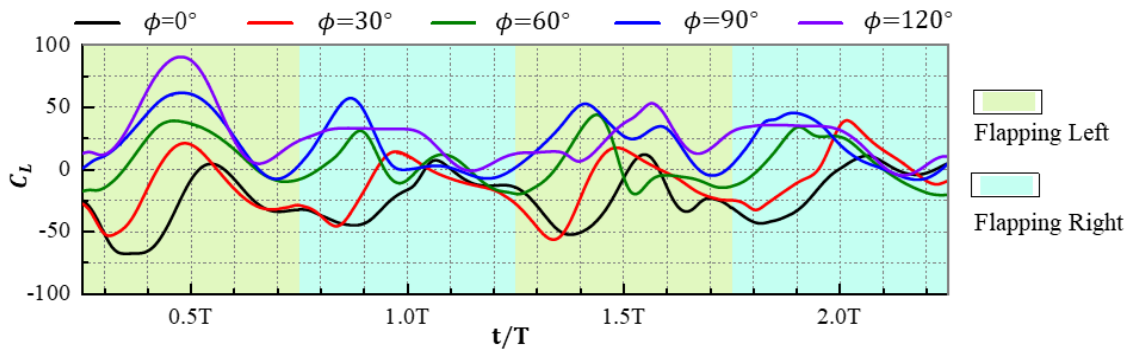
**Fig. 13 Lift coefficient curve with different phase difference**
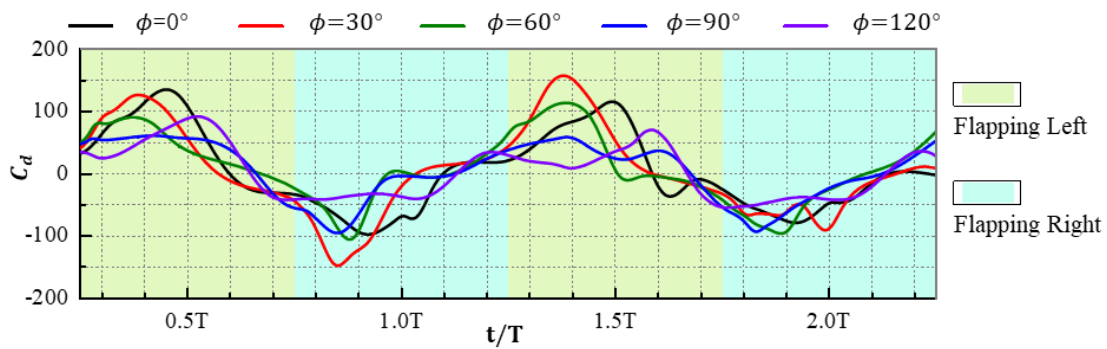


**Fig. 14 Drag coefficient curves of different phase differences**

### 3.2 Influence of Translational Motion and Rotating Motion

The aerodynamic characteristics in four working conditions with $\phi$ =0°, 30°, 60°, 90° and 120° are studied in this section accordance with Eq. (12) when the incoming flow $u$ =0.6m/s. Other flapping structure parameters and flapping frequency are same with them mirrored in Table 2. The lift coefficient curves with different phase differences are represented in Fig. 13, and drag coefficient curves are displayed in Fig. 14.

As can be seen from Fig. 13, there are obvious differences in the lift coefficient curve values of flapping wings with different phase differences. By comparing the peak and valley values of lift coefficient curve, when phase difference of flapping wings is 0°, 30°, 60° and 90°. It can be seen that peak and valley values move upward to left. When the phase difference is 0° in one flapping period, the flapping wing lift coefficient curve is basically below the $x$ at 30° and downward negative lift force is produced by the flapping wing periodic flapping. As the flapping wing phase difference is 60°, the flapping wing lift coefficient curve fluctuates around the $x$. And when the flapping wing phase difference is 90° and 120°, the flapping wing lift coefficient curve is basically above the $x$. Upward positive lift force is generated by periodic flapping.

In this paper, the drag of flapping wing is positive to right. From Fig. 14, when wing flaps to the left, drag coefficient curve is above $x$ in most of time and wing is resisted to right in a large part of the time. In a small part of time, the curve is below $x$, and flapping wing is subject

to drag to left. The situation is similar when flapping to the right, but the drag direction is different. In each stroke, the drag of the flapping wing is generally increased first and the decreased. As a result, a convex curve is formed when the flapping wing flaps to the left and a concave curve is formed as it flaps to the right. And the peak and valley values of the curve are steeper and the peak value of the curve is larger when the phase difference is 0°, 30° and 60°. At 90° and 120°, the peaks and valleys of the curve are relatively smooth, and the peak values of the curve are relatively small. With different phase differences of flapping wing, the corresponding peak time of its lift coefficient curve is different.

The periodic average value of the flapping wing lift and drag coefficient is depicted in Table 3. Fig. 15 is line chart of the periodic average value of flapping wing lift and drag coefficient. From Table 1 and Fig. 15, when the incoming flow $u$=0.6m/s, $\bar{C}_{L(T)}$ of increases as the phase difference increases from 0° to 120°. When $\phi$ is 0° and 30°, $\bar{C}_{L(T)}$ is negative, and wing is affected by the downward negative lift. When $\phi$ is 60°, 90° and 120°, $\bar{C}_{L(T)}$ is positive, and wing is affected by the upward lift. When $\phi$ is 120°, $\bar{C}_{L(T)}$ the largest, and when $\phi$ is 0°, $\bar{C}_{L(T)}$ is the smallest. When $\phi$ is 120°, $\bar{C}_{L(T)}$ increases by 212% compared with 0°. When $\phi$ is 0°, 30°, 60°, 90° and 120°, $\bar{C}_{D(T)}$ is positive then wing is subjected to the right when periodic flapping, indicating that flapping wing cannot fly forward with incoming velocity. When $\phi$ increases from 0° to 120°, $\bar{C}_{D(T)}$ increases first and then decreases. When $\phi$ is 60°, $\bar{C}_{D(T)}$ is the largest, and when $\phi$ is 90°, $\bar{C}_{D(T)}$ is
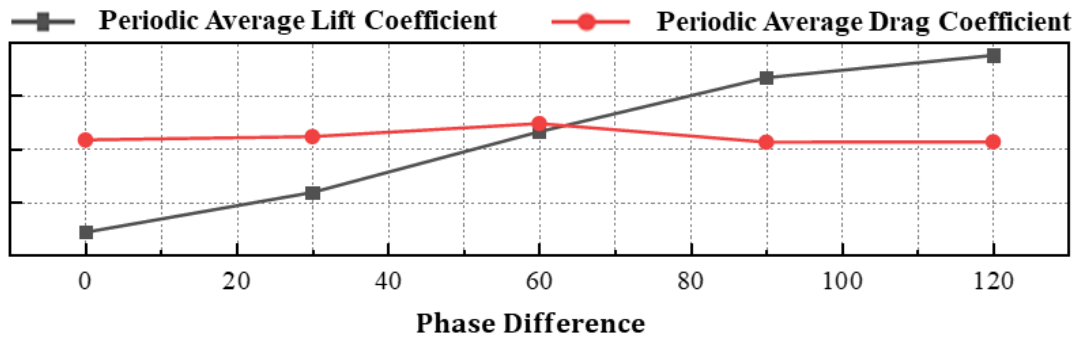
**Fig. 15 Line chart of periodic mean value of lift and drag coefficient with different phase difference**
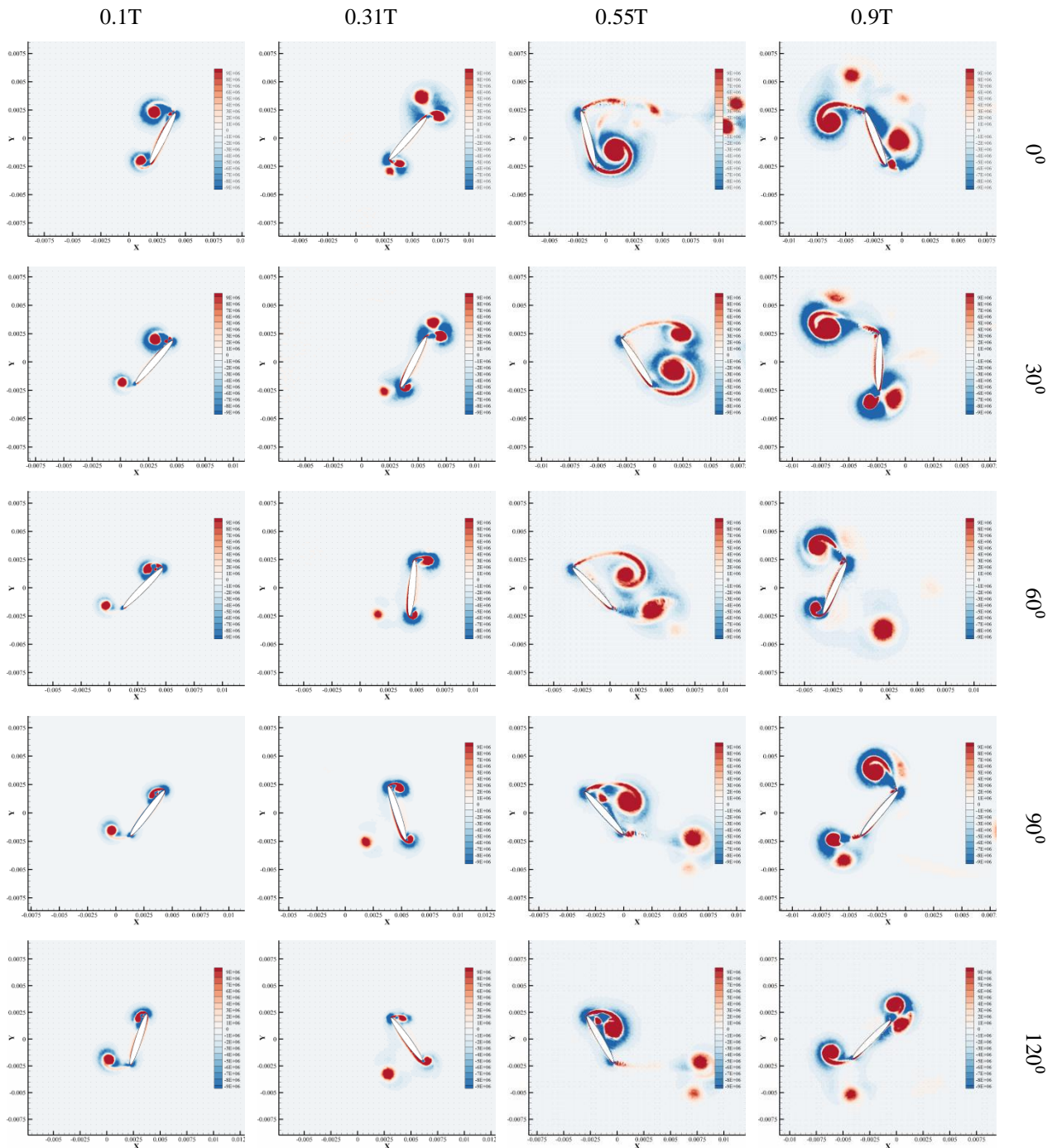


**Fig. 16 Vorticity contour of flapping wing flow field (Q criterion)**

|  | 0.1T | 0.31T | 0.55T | 0.9T |
|---|---|---|---|---|
| 0° | | | | |
| 30° | | | | |
| 60° | | | | |
| 90° | | | | |
| 120° | | | | |
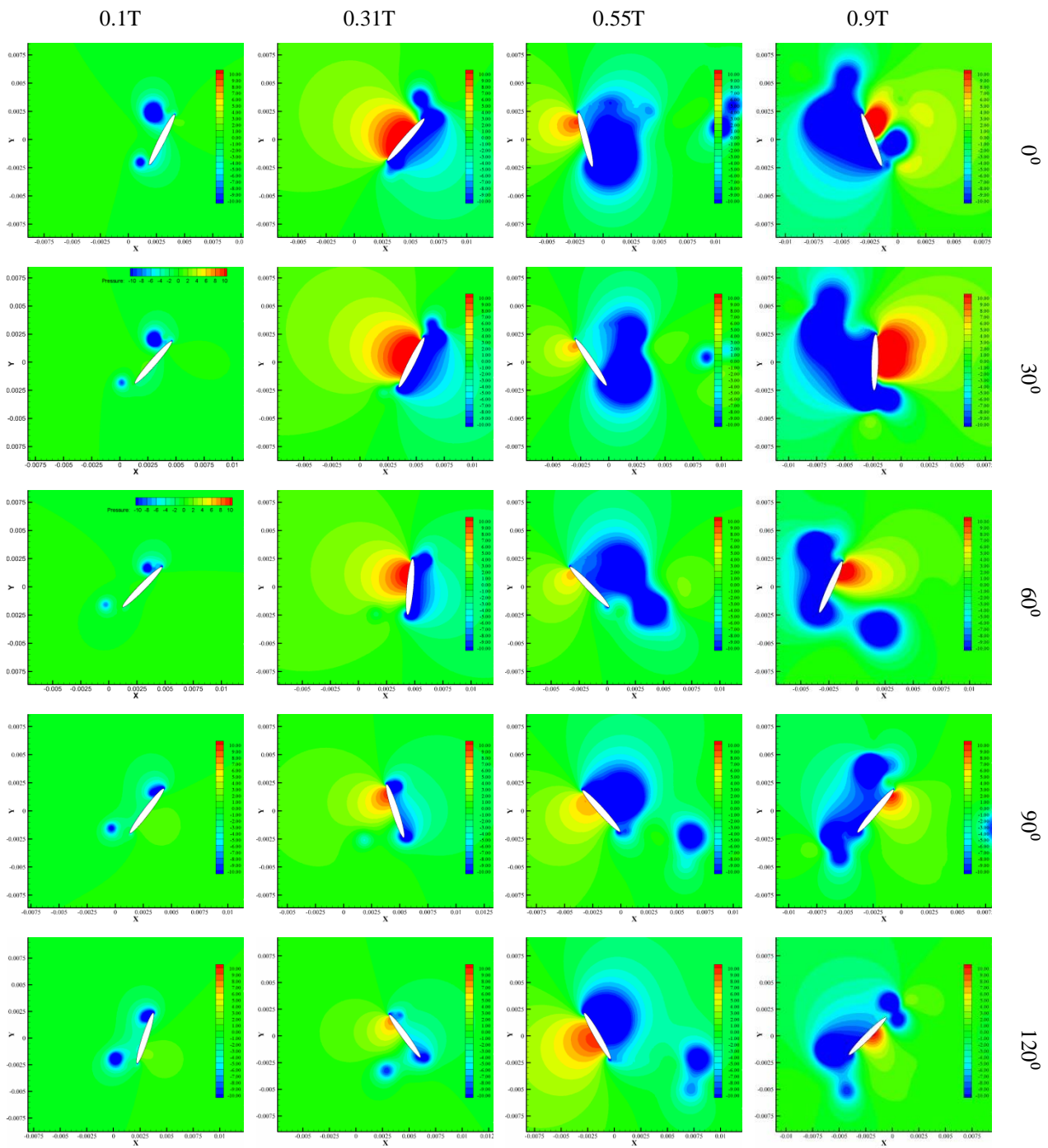
**Fig. 17 Pressure contour of flapping wing flow field**

**Table 3 Periodic average values of lift and drag coefficients for different phase differences**

| $\phi$ | $\bar{C}_{L(T)}$ | $\bar{C}_{D(T)}$ | $\bar{C}_{L(T)}/\bar{C}_{D(T)}$ |
|---|---|---|---|
| 0° | -23.4508 | 2.542039 | -9.22518 |
| 30° | -12.3082 | 3.476879 | -3.54002 |
| 60° | 4.838572 | 7.155596 | 0.676194 |
| 90° | 20.00656 | 1.904612 | 10.50427 |
| 120° | 26.33788 | 2.015788 | 13.0658 |

the smallest. When $\phi$ is 60°, $\bar{C}_{D(T)}$ is about 3.76 times that of 90°.

Figure 16 and Fig. 17 are vorticity and pressure of the flow field with different phase differences, respectively. It is indicated from Fig. 16 and Fig. 17 that at 0.1T, as the phase difference rises from 0° to 120°, the adhesion of leading-edge vortex on upper airfoil continuously increases. At 0.31T, the attack angle with different phase difference is different, and the attack angle of 0° and 30° is negative. The attack angle is positive for flapping wings with phase difference of 90° and 120°. At 0.31T, the leading-edge vortex and wake vortex capture occurred on flapping wing, and low-pressure area on the leading-edge became stronger. With phase difference of 0° and 30° at 0.55T, low-pressure area at trailing edge of upper-wing surface is stronger through trailing-edge vortex. While

low-pressure area at leading-edge is not strong, leading-edge vortex adhesion is not strong and falls off, trailing-edge vortex adhesion becomes stronger and adheres to trailing edge of the upper-wing surface. The leading-edge vortex with phase difference of 90° and 120° are stronger, which attach to the upper airfoil area at the leading-edge of flapping wing. Then low-pressure area of upper airfoil is strengthened and trailing-edge vortex shed, by which is affected on low-pressure area of upper airfoil. It is illustrated in the above phenomena that adhesion and strength of the leading-edge and trailing-edge vortex of flapping wing can be affected by the phase difference through altering the attack angle. And then low-pressure area of upper airfoil is influenced, and finally aerodynamic characteristics is affected.

### 3.3 Influence of Different Trajectories of Flapping Wing

At this segment, the aerodynamic characteristics of with horizontal linear trajectory, 45° inclined linear trajectory, elliptical trajectory and "∞" trajectory are investigated when the longitudinal incoming flow $u$=0.6m/s. The flapping structure parameters and flapping frequency are identical with them shown in Table 2. The trajectory motion equation of four kinds of flapping wing in this paper is as follows:

1) Horizontal linear motion equation and motion trajectory is:

$$\begin{cases} h(t) = h_a \sin(2\pi ft) \\ \alpha(t) = \alpha_0 - \alpha_a \sin(2\pi ft + \phi) \end{cases} \tag{13}$$

The horizontal linear motion trajectory of the flapping wing is shown in Fig. 18.

2) The motion equation and motion trajectory of elliptic trajectory is:

$$\begin{cases} x(t) = h_a \sin(2\pi ft) \\ y(t) = 0.1h_a \cos(2\pi ft) \\ \alpha(t) = \alpha_0 - \alpha_a \sin(2\pi ft + \phi) \end{cases} \tag{14}$$
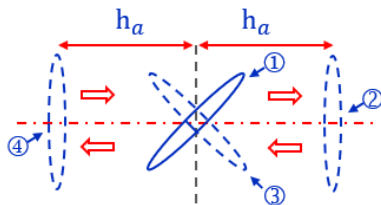


**Fig. 18 Horizontal linear motion trajectory of centroid**
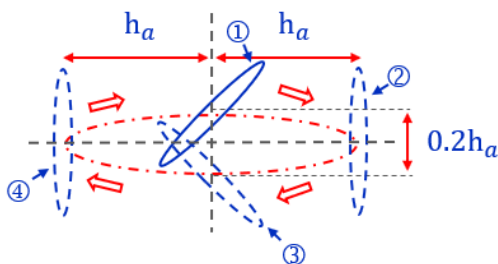


**Fig. 19 Elliptical motion trajectory of centroid**
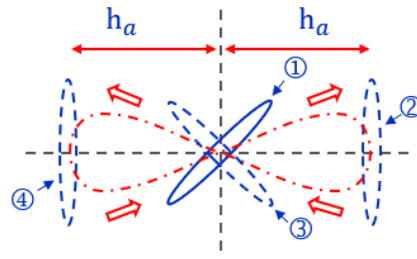


**Fig. 20 "∞" shape motion trajectory of centroid**
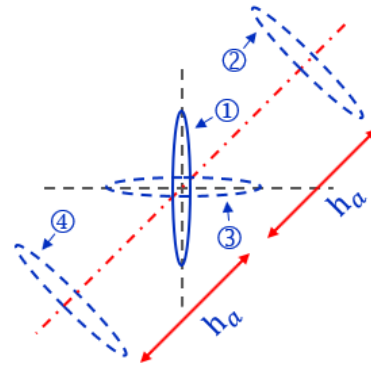


**Fig. 21 Linear motion trajectory with 45 ° inclination of mass center**

The elliptical motion trajectory diagram is portrayed in Fig. 19.

3) The motion equation and motion trajectory of "∞" shape is:

$$\begin{cases} x(t) = h_a \sin(2\pi ft) \\ y(t) = 0.2h_a \sin(2\pi ft)\cos(2\pi ft) \\ \alpha(t) = \alpha_0 - \alpha_a \sin(2\pi ft + \phi) \end{cases} \tag{15}$$

The motion trajectory of "∞" shape is depicted in Fig. 20.

4) The motion equation and motion trajectory of 45° oblique line is:

$$\begin{cases} x(t) = \frac{\sqrt{2}}{2}h_a \sin(2\pi ft) \\ y(t) = \frac{\sqrt{2}}{2}h_a \sin(2\pi ft) \\ \alpha(t) = \alpha_0 - \alpha_a \sin(2\pi ft + \phi) \end{cases} \tag{16}$$

The 45° oblique motion trajectory is presented in Fig. 21.

The calculated lift coefficient curves of flapping wings with different trajectories are reflected in Fig. 22. Based on the content of this paper, it can be seen that there are some high lift mechanisms in the flapping process of flapping wings. Under the effect of the lift mechanism, lift coefficient curve will rise, and after the end of the lift mechanism, lift coefficient curve will decline, so the lift coefficient curve changes. From Fig. 22, $C_L$ of the horizontal straight track, elliptical track and "∞" shape track is positive for most of the time when the flapping wing flaps left and right, by which lift force is generated. During the term from the end of previous stroke to the
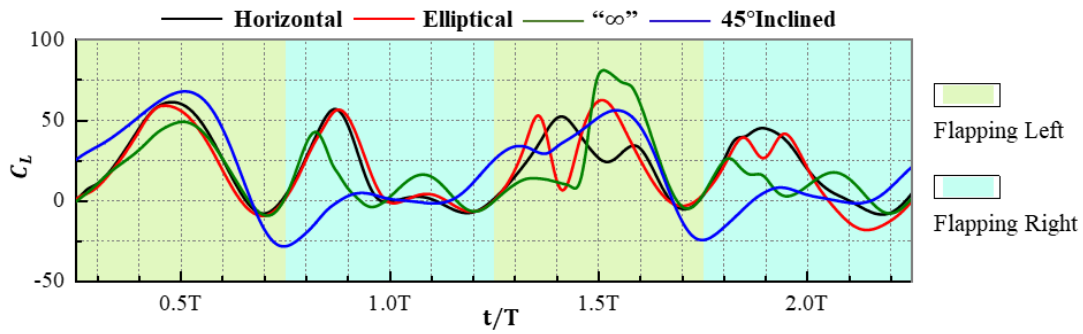
Fig. 22 Lift coefficient of flapping wing in different trajectories
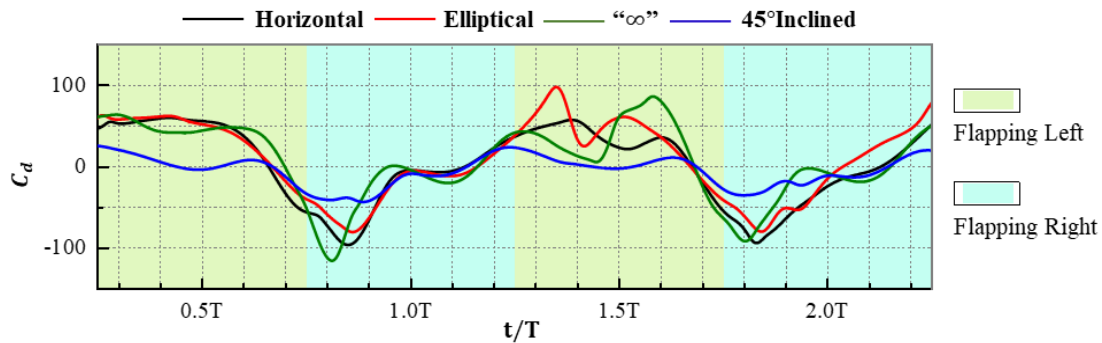


Fig. 23 Drag coefficients of flapping wings in different trajectories

Table 4 Periodic average value of lift and drag coefficient

| Trajectory Type | $\bar{C}_{L(T)}$ | $\bar{C}_{D(T)}$ | $\bar{C}_{L(T)}/\bar{C}_{D(T)}$ |
|---|---|---|---|
| Elliptical | 18.70924087 | 9.566086605 | 1.955788364 |
| "∞" Shape | 17.34578421 | 6.124628447 | 2.832136572 |
| 45° Inclined | 16.33037622 | -5.379171987 | -3.035853149 |
| Horizontal | 20.00773463 | 1.900884436 | 10.52548711 |

beginning of new stroke, $C_L$ of flapping wing is below the $x$, and then negative lift force is generated by flapping. The lift coefficient curves of the 45° inclined linear trajectory are obviously different from those of other trajectories. Strong lift force is produced by flapping wing when it flaps to the left and down, but weak lift force when it flaps to the right and up. In view of the above phenomenon, it is believed in this paper that the lift component of the flapping wing in the direction $y$ is made lager by airfoil attitude angle when the flapping wing is flapping to the left along the 45° oblique linear trajectory. And the drag (or thrust) component in the positive direction $x$ smaller. While when the flapping is in the upper right direction, the lift component in the $y$ direction is made smaller or even negative by the airfoil attitude angle. And the drag (or thrust) component in the $x$ positive direction larger.

The drag coefficient curves of flapping wings with different trajectories are represented in Fig. 23. The drag force will be produced to the right most of the time by flapping wings with different trajectories when they flap to the left, and drag force to the left most of the time when they flap to the right. When this stroke is about to end and the next stroke begins, drag force in the same direction as

the flapping will be generated. Greater drag force will be produced by horizontal linear trajectory, elliptical trajectory and "∞" shape trajectory drag coefficient curve when the left and right flapping. 45° oblique trajectory drag coefficient is smaller when the left flapping down, the drag coefficient is larger when the right flapping up. Other trajectory drag coefficient curves are also significantly different.

Under the provisions of longitudinal incoming flow, the periodic average values of lift coefficient and drag coefficient of flapping wings are mirrored in Table 4. The $\bar{C}_{L(T)}$ of flapping wings with horizontal linear trajectory is largest, while that of flapping wings with 45° oblique trajectory is smallest, and $\bar{C}_{L(T)}$ with horizontal linear trajectory is about 1.22 times of 45°. The $\bar{C}_{D(T)}$ of horizontal linear trajectory, elliptical trajectory and "∞" shape trajectory are all positive, indicating that the flapping wing cannot fly left in the flow field according to the given flow velocity. The $\bar{C}_{D(T)}$ of the 45° inclined linear trajectory is negative, which means that the flapping wing can fly to the left in this flow field at this moment.

When the longitudinal incoming flow $u$ is 0.6m/s, the flow field cloud diagrams of the four kinds of flapping
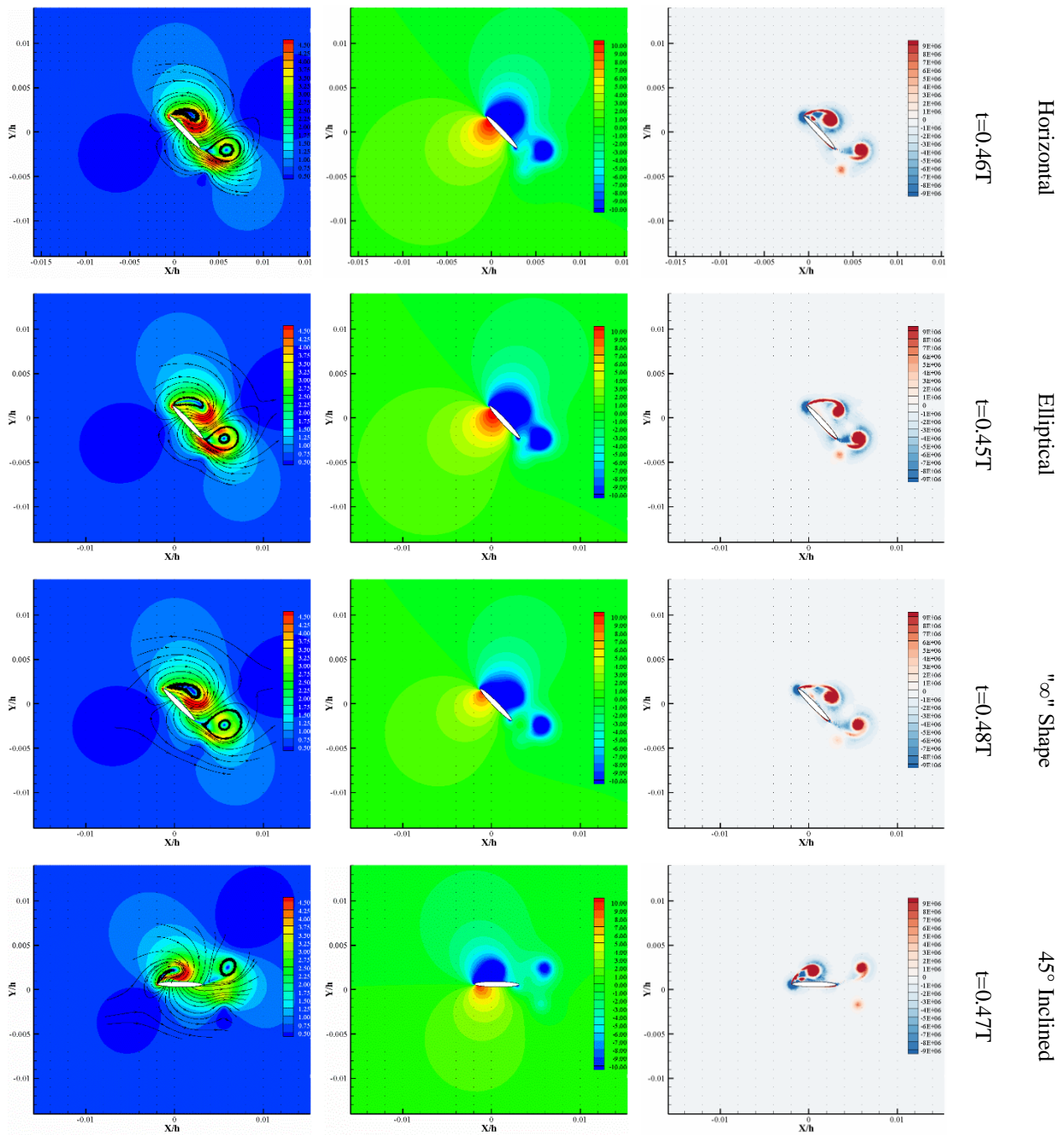
**Fig. 24 Contour of leading-edge vortex stall mechanism, velocity contour on the left, intermediate pressure contour and vorticity contour on the right (Q criterion)**

wing movement paths are portrayed in Fig. 24 and Fig. 25. In the flow fields of the four kinds of flapping wing movement paths, there are both delayed stall lift mechanism of leading-edge vortex and wake vortex capture mechanism. The difference is that leading-edge vortex intensity and low-pressure area of upper-wing surface are different. Angle between horizontal linear trajectory, elliptical trajectory, and "∞" shape trajectory flapping wing and the horizontal plane is roughly the same. In contrast, the angle between 45° inclined linear trajectory flapping wing and the horizontal plane is obviously different from the first three. The reason that the difference of $C_L$ can be explained by the above phenomenon.

### 3.4 Influence of Chordwise Flexibility

It is assumed in all the previous studies that the flapping wing is rigid, that is, the flapping wing will not deform during flight, or the deformation is small enough to be ignored. At present, the influence of flapping wing flight flexibility deformation is still not very clear, and further research and further improvement of the theory of flapping wing flexibility are needed. In this section, the active bending deformation flexible flapping wing is numerically researched.

In this section, active deformation is mainly applied to the airfoil according to literature (Olivier & Dumas, 2016), and the influence of active flexible deformation on
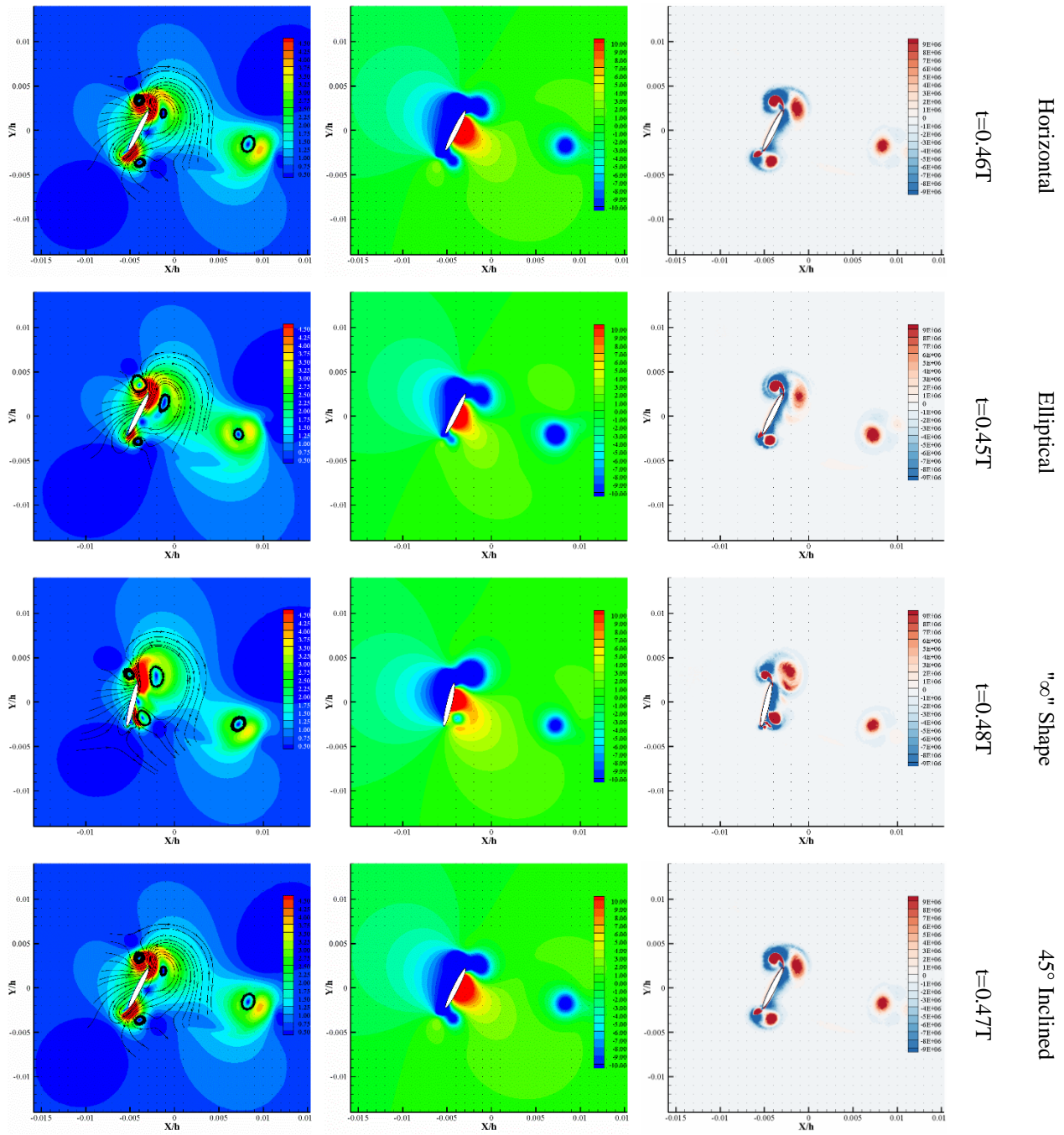
**Fig. 25 Contour of wake capture mechanism, velocity contour on the left, intermediate pressure contour, vorticity contour on the right (Q criterion)**

the aerodynamic characteristics of the airfoil is explored. The deformation function is as follows:

$$f(x) = -a_0 x^2 \cos(2\pi f t + \psi) \qquad (17)$$

Where $a_0$ is the maximum deformation amplitude of flapping wing trailing edge and $\psi$ is the phase angle between flapping and deformation of airfoil. The specific research content is the influence of deformation amplitude $a_0$ on flapping wing flight as $\psi = 0$. When the translation speed is the largest, the flexible deformation is the largest. The flapping wing is elliptical, the wingspan string length is $h$, and the maximum thickness of the wingspan is $0.02h$. According to Eq. (12), the flapping wing moves in incompressible air. The flow field of the flapping wing

under three conditions $a_0$ of $6.3\,h$, $3.16\,h$ and $0$ is numerically calculated using FMV. The flexible deformation of airfoil during the whole numerical study is shown in Fig. 26.

When the incoming flow $u = 0.6$m/s, the flapping wing is flexibly deformed according to Eq. (17), and the aerodynamic characteristics of flapping wing movement in the air are performed according to Eq. (12). The flow field $a_0$ of $6.32h$, $3.16h$ and $0$ is calculated by FMV. The lift coefficient and drag coefficient of the flapping wing are shown in Fig. 27 and 28. It can be seen that with the advance of time, the differences among the lift and drag coefficient curves of different flexible wings are made obvious constantly.
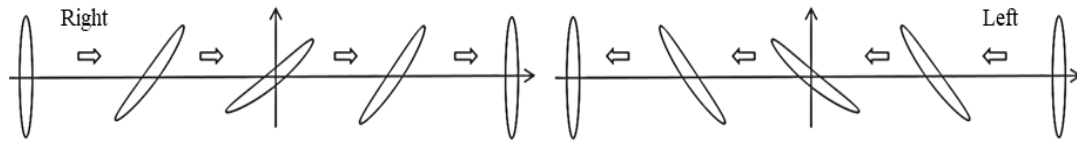
**Fig. 26 Schematic diagram of flexible deformation**
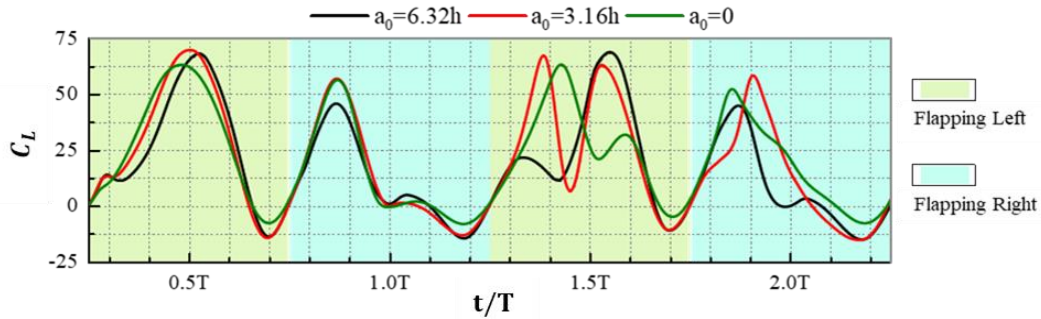


**Fig. 27 Lift coefficient curve**
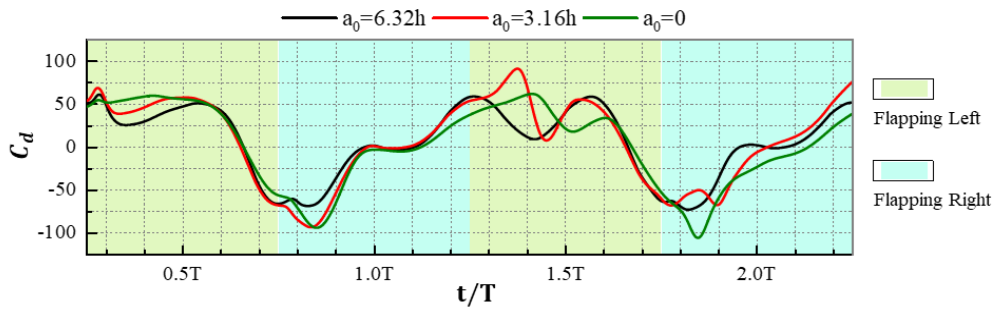


**Fig. 28 Resistance coefficient curve**

**Table 5 cycle average lift and drag coefficient**

| $a_0$ | $\bar{C}_{L(T)}$ | $\bar{C}_{D(T)}$ | $\bar{C}_{L(T)}/\bar{C}_{D(T)}$ |
|-------|------------------|------------------|----------------------------------|
| $6.32h$ | 16.8430261 | 5.699715482 | 2.955064362 |
| $3.16h$ | 19.61547294 | 7.569777515 | 2.591287908 |
| 0 | 20.54722645 | 2.002557666 | 10.26049177 |

It can be observed from Fig. 27 and 28 that the peak and valley values of the lift and drag coefficient curves of the flexible deformed flapping wing are larger than those of the rigid flapping wing, indicating that the leading-edge vortex generated by the flapping wing movement is impacted by the flexible deformation. The peak values of $C_L$ and $C_D$ of each flapping wing in the second flapping cycle are obviously different. This is because the wake vortex capture mechanism of $a_0 = 3.16h$ and 0 of the flapping wings is strong, while the wake vortex capture mechanism of $a_0 = 6.32\ h$ is not strong. Then the difference in the second peak is due to the difference in the intensity of the leading-edge vortex in the stroke for delayed stall mechanism of the leading-edge vortex.

As is shown in Table 5 that when the incoming flow $u = 0.6$m/s, $\bar{C}_{L(T)}$ is the largest at $a_0 = 0$, followed by $a_0 = 3.16h$, and the smallest at $a_0 = 6.32h$. It is seen that

$\bar{C}_{L(T)}$ of the flapping wing will be reduced through increasing the chordwise flexibility of the flapping wing. When the incoming flow $u = 0.6$m/s, positive $\bar{C}_{D(T)}$ of different flexible flapping wings are obtained, indicating that the thrust to the right is exerted on the flapping wings and the flapping wings cannot fly in the flow field according to the incoming flow speed.

## 4. CONCLUSION

In this paper, some motion parameters of flapping wing flight are studied, flapping wing flight is divided into several stages, and it is found that there is interaction between lift mechanisms of flapping wing flight:

(a) The lift resistance characteristics of the flapping wing can be improved through increased frequency of flapping wing, because the strength and adhesion of leading-edge vortex and trailing-edge vortex are possible to be enhanced through increasing frequency. The low-pressure area of upper-wing surface can be made stronger by it.

(b) The attack angle of the airfoil can be affected by the phase difference during flapping. The attack angle of the airfoil can be made negative through some phase

difference, such as $0^0$ phase difference in this paper, and the negative lift can be generated by airfoil flapping. The attack angle of the airfoil can be made positive through the $90^0$ phase difference, and the positive lift can be generated by airfoil flapping.

(c) When flapping frequency, amplitude and phase difference are same, lift characteristics of the flapping wings with elliptical trajectory, horizontal linear trajectory and "∞" shape trajectory are not different, and the drag coefficients are different greatly. When the maximum flapping stroke is the same, the frequency and phase difference are also the same, the axial symmetry of the motion trajectory is different, and the lift characteristics will be significantly different.

(d) Several limitations are presented in this paper. A sinusoidal function is selected as the flap rotation function, which represents a relatively simplistic mathematical model of flap motion. The trapezoidal function can be utilized as the rotation function or a mathematical model that can more accurately simulate the actual flapping motion may be constructed in future research. The chordwise flexible flapping wing is concentrated on in this study, and the active flexibility of the wing is applied based on a given formula. However, further investigation regarding the passive flexibility of the flapping wing is required. In a three-dimensional context, the chordwise and spanwise flexibility of the flapping wing, as well as the impact of the flapping wing curvature characteristics on its aerodynamic characteristics, need to be further explored.

## CONFLICT OF INTEREST

Author declares there are no conflicts of interest.

## AUTHORS CONTRIBUTION

**Ziyu Guo:** Visualization, Writing, Methodology; **Ruidong Liu:** Conceptualization, Investigation; **Shizhen Zheng:** Investigation, Software; **Junjie Xu:** Formal analysis, Data Curation; **Jianlong Chang:** Writing-review, Resources, Project administration.

## REFERENCES

Arranz, G., Flores, O., & Garcia-Villalba, M. (2020). Three-dimensional effects on the aerodynamic performance of flapping wings in tandem configuration. *Journal of Fluids and Structures*, *94*, 102893. https://doi.org/10.1016/j.jfluidstructs.2020.102893

Bhat, S. S., Zhao, J., Sheridan, J., Hourigan, K., & Thompson, M. C. (2020). Effects of flapping-motion profiles on insect-wing aerodynamics. *Journal of Fluid Mechanics*, *884*, A8. https://doi.org/10.1017/jfm.2019.929

Gonzalo, A., Arranz, G., Moriche, M., Garcia-Villalba, M., & Flores, O. (2018). From flapping to heaving: A numerical study of wings in forward flight. *Journal of Fluids and Structures*, *83*, 293-309. https://doi.org/10.1016/j.jfluidstructs.2018.09.006

Han, J. S., Tuan Nguyen, A., & Han, J. H. (2019). Aerodynamic characteristics of flapping wings under steady lateral inflow. *Journal of Fluid Mechanics*, *870*, 735-759. https://doi.org/10.1017/jfm.2019.255

Huang, H. F., Chen, Z., He, W., Li, Q., & Niu, T. (2024). Aerodynamic analysis and flight control of a butterfly-inspired flapping-wing robot. *Ieee Robotics and Automation Letters*, *9*(11), 9677-9684. https://doi.org/10.1109/lra.2024.3458591

Jiaolong, Z., Jun, H., & Yong, Y. (2017). *Flow structure and mechanics property of flapping wing at different reduced frequency*. Chinese Mechanics Conference-2017 and Celebration of the 60th Anniversary of the Chinese Mechanics Society, Beijing, China.

Jin, B. R., Wang, L., Ravi, S., Young, J., Lai, J. C. S., & Tian, F. B. (2024). Enhancing tip vortices to improve the lift production through shear layers in flapping-wing flow control. *Journal of Fluid Mechanics*, *999*, 33, A25. https://doi.org/10.1017/jfm.2024.942

Lee, H., Jang, J., Wang, J., Son, Y., & Lee, S. (2019). Comparison of cicada hindwings with hindwing-less drosophila for flapping motion at low Reynolds number. *Journal of Fluids and Structures*, *87*, 1-22. https://doi.org/10.1016/j.jfluidstructs.2019.02.015

Lee, N., Lee, S., Cho, H., & Shin, S. (2018). Effect of flexibility on flapping wing characteristics in hover and forward flight. *Computers & Fluids*, *173*, 111-117. https://doi.org/10.1016/j.compfluid.2018.03.017

Ma, D. F., Song, B. F., Gao, S. J., Xue, D., & Xuan, J. L. (2024). Designing efficient bird-like flapping-wing aerial vehicles: insights from aviation perspective [Review]. *Bioinspiration & Biomimetics*, *19*(6), 27, 061001. https://doi.org/10.1088/1748-3190/ad88c4

McMichael, J. M. (1997). Micro Air vehicles-toward a new dimension in flight. *http://www.arpa.gov/tto/MAV/mav_auvsi.html*. https://cir.nii.ac.jp/crid/1573950399959036928

Olivier, M., & Dumas, G. (2016). Effects of mass and chordwise flexibility on 2D self-propelled flapping wings. *Journal of Fluids and Structures*, *64*, 46-66. https://doi.org/10.1016/j.jfluidstructs.2016.04.002

Shyy, W., Trizila, P., Kang, C. K., & Aono, H. (2009). Can tip vortices enhance lift of a flapping wing? [Editorial Material]. *Aiaa Journal*, *47*(2), 289-293. https://doi.org/10.2514/1.41732

Srinidhi, N. G., & Vengadesan, S. (2017). Ground effect on tandem flapping wings hovering. *Computers & Fluids*, *152*, 40-56. https://doi.org/10.1016/j.compfluid.2017.04.006

Tay, W. B. (2017). Effect of different types of wing-wing interactions in flapping MAVs. *Journal of Bionic Engineering*, *14*(1), 60-74. https://doi.org/10.1016/s1672-6529(16)60378-5

Trizila, P., Kang, C. K., Aono, H., Shyy, W., & Visbal, M. (2011). Low-Reynolds-number aerodynamics of a flapping rigid flat plate [Proceedings Paper]. *AIAA Journal*, *49*(4), 806-823. https://doi.org/10.2514/1.J050827

Verma, A., & Kulkarni, V. (2024). Monitoring the wake of low reynolds number airfoils for their aerodynamic loads assessment. *Journal of Applied Fluid Mechanics*, *17*(11), 2481-2498. https://doi.org/10.47176/jafm.17.11.2607

Wang, Y., He, X., He, G., Wang, Q., Chen, L., & Liu, X. (2022). Aerodynamic performance of the flexibility of corrugated dragonfly wings in flapping flight. *Acta Mechanica Sinica*, *38*(11). https://doi.org/10.1007/s10409-022-22038-x

Wu, J., Chen, L., Zhou, C., Hsu, S. J., & Cheng, B. (2019). Aerodynamics of a Flapping-Perturbed Revolving Wing. *AIAA Journal*, *57*(9), 3728-3743. https://doi.org/10.2514/1.J056584

Xiansheng, H., Yu, C., Qi, L., & Bin, L. (2023). Research and test of X-Wing flapping-wing mechanism based on the crank slider mechanism. 47(03), 57-64. https://doi.org/10.16578/j.issn.1004.2539.2023.03.008